Solving Navier–Stokes equation for flow past cylinders using single-block structured and overset grids

Tapan K. Sengupta *, V.K. Suman, Neelu Singh

Department of Aerospace Engineering, IIT Kanpur, UP 208 016, India

ABSTRACT

Many complex fluid motions are driven by physical processes of instability, transition and turbulence dependent upon nonlinear mechanisms. Here, we solve the flow past cylinder(s) using single-block structured and overset grids by computing Navier–Stokes equation in two-dimensions. The suitability of a compact scheme in discretizing convection and diffusion terms are investigated first by looking at relevant numerical properties. Also, for the overset grid method, one of the methods is identified that shows the best results in minimizing interpolation error at sub-domain boundaries for an analytical test function. We provide extensive comparisons with experimental and other computational results for flow past a single cylinder, utilizing both single-block structured and Chimera or overset grids. Apart from showing instability of this flow calculated by these methods, we also compare the computed vorticity and velocity data using these two grids by employing the proper orthogonal decomposition (POD). We have analyzed and developed an overset grid method with compact scheme that does not need any filtering to control error. This has been ascertained by performing POD analysis. To show that the developed method is capable of handling complex geometries, we have computed flow past two cylinders in side-by-side arrangement. Results obtained capture the known flow characteristics for this arrangement well using relatively fewer number of grid points.

© 2009 Elsevier Inc. All rights reserved.

1. Introduction

Numerical instability for the solution of partial differential equations has many common features with nonlinear instability of hydrodynamics problems [1]. Thus, it is desirable to characterize numerical methods based on their ability to compute proto-typical nonlinear flow instability problems. In this context, vortex shedding behind a circular cylinder constitutes an ideal example, which is known for its initial linear instability followed by super-critical nonlinear saturation.

In flow past a cylinder started impulsively, one notes the formation of symmetric recirculation regions at the base of the geometry. These wake bubbles grow in width and length with time, retaining the top-down symmetry. In the early stages of flow evolution, increase in time is equivalent to increase in Reynolds number and this is seen in all flows past a cylinder following the impulsive start at all Reynolds numbers. For flows above a critical Reynolds number (Re_{cr}), an asymmetry in the wake bubble develops leading to alternate growth of the bubbles and eventual shedding, forming the Bènard–Kàrmàn street. Experimentally, it is noted that the time at which this asymmetry occurs is a function of Reynolds number. In addition to alternate vortices in the Bènard-Kàrmàn street, researchers in [2–6] have reported experiments in detection of 2D waves in the separated shear layer in the Reynolds number range 1000–50,000 as quoted in [7]. According to Braza et al. [7], these

---

* Corresponding author.
  E-mail address: tksen@iitk.ac.in (T.K. Sengupta).

specific waves are created by the Kelvin–Helmholtz instability of the separated shear layer. Vortex shedding starts via temporal linear instability and the final limit cycle-like oscillations result from nonlinear super-critical stability of the flow, that has often been described by the Landau model [8,9].

Many researchers [10–12] have studied the linear instability of this flow as a Hopf bifurcation problem and reported a critical Reynolds number between 45 and 46. By definition, Hopf bifurcation refers to a phenomenon in which a steady state flow evolves into a time-periodic state as a bifurcation parameter is varied [13]. For numerical investigations with Reynolds number as the bifurcation parameter, a critical value is identified when the system is unimpeded by noise (other than those due to discretization and round-off). Experimentally observed critical Reynolds number values reported in the literature show quite a large scatter [14–18]. Difference between the Hopf bifurcation critical Reynolds number and the experimental Re_{cr} is related to the facility-dependent background disturbances.

Landau equation [8,9] can explain the super-critical stability following the primary linear temporal instability of a single normal mode, for flow past a circular cylinder. Here the disturbance is expressed as, $u'(\vec{X}, t) = A(t)f^*(\vec{X}) + A^*(t)f(\vec{X})$, where quantities with asterisks denote complex conjugate of the function. If the complex amplitude for perturbation is expressed as $A(t) = \text{Const} \cdot e^{\sigma_1 t} e^{i\omega_1 t}$, then the time variation of amplitude for linear problem is given by, $\frac{d|A|^2}{dt} = 2\sigma_1 |A|^2$. Landau extended it to nonlinear problem by retaining the nonlinear self-interaction term to obtain [8,9],

$$\frac{d|A|^2}{dt} = 2\sigma_1 |A|^2 - l|A|^4, \tag{1}$$

where l is the Landau coefficient that was originally considered as real. Solution to this equation is readily obtained when $l > 0$ and $\sigma_1 > 0$ as given in [9],

$$|A|^2 = \frac{A_0^2}{(A_0/A_e)^2 + [1 - (A_0/A_e)^2]e^{-2\sigma_1 t}}, \tag{2}$$

where A_0 is the value of A at $t = 0$. Here, $A_e = (2\sigma_1/l)^{1/2}$ represents the asymptotic value of the solution for $t \to \infty$. Note the condition $\sigma_1 > 0$ corresponds to the case when the Reynolds number exceeds the critical value Re_{cr}, associated with linear instability. Approach of A to A_e, indicates independence of A_e on A_0. Such a solution is due to particular combination of the Landau coefficient (l), being real and positive and Re greater than Re_{cr} that takes the temporally growing flow to a strictly time periodic neutral state. This is thus, a case of *super-critical stability*. Occurrence of super-critical state indicates the central role played by nonlinearity in determining the eventual limit cycle. Although the Landau model suggests that there is no role played by background disturbances on A_e (unless l depends on input disturbances), the initial linear temporal instability depends upon the receptivity aspect, i.e. upon the presence of relevant disturbance field at the relevant length and time-scales. For flow past a cylinder, eventual vortex shedding depends upon the background disturbance spectrum. This is strongly indicated by different Re_{cr} reported from different experimental facilities.

The Landau model has been probed experimentally independently in [19,20] and the authors reported experimentally measured parameters of the Landau equation. Interestingly, in Fig. 3 of [19] and in Fig. 6 of [20], different values of Re_{cr} have been reported for cylinders with different L and D of the cylinder model. Similar variations of Re_{cr} were also reported earlier in [21] and all the authors have concluded that this is essentially due to different aspect ratio of the models, as the same tunnel is used for all the experiments in respective references. Thus, the difference in the values of Re_{cr} was attributed to three-dimensionality of the flow field, despite the fact that the models used were for wall to wall in the tunnel. However, this contradicts the observation in [22], which stated clearly that the flow remains essentially two-dimensional for Re kept less than 180. The alternative explanation was proposed in [23] where the authors argued and experimentally demonstrated that the background disturbance in a given tunnel is a function of tunnel speed. Specifically, they showed that if a Reynolds number of 53 was obtained using two cylinders of diameters 5 mm and 1.8 mm, then the corresponding tunnel speeds were 17 cm/s and 46.9 cm/s. At these two speeds the background disturbances at Strouhal frequency differed by a factor of 10. This difference showed up as a strong shedding at the lower speed and almost weak or absent shedding for the higher speed. Thus, the initial temporal instability (or the receptivity) can occur if the background disturbance is strongly present at the Strouhal frequency. This is also the likely scenario for the experiments in [19–21], where different aspect ratio cylinders were used in the same tunnels, but the coupling between free stream turbulence with speed for different diameter cylinders was not studied. Although the variation of equilibrium amplitude with free stream turbulence level was presented in Fig. 14 of [20] that shows quite a large scatter of the growth rate with Re in the range between 50 and 60. In fact, the results for larger turbulence levels show Re_{cr} that is significantly higher than the value between 45 and 46 often quoted in the literature.

While it is not too difficult to match computed results with other numerical and experimental results for the drag coefficient and the Strouhal number [22,24,25], a more difficult task is to compare the asymptotic fluctuating lift amplitude whose value is as given above by A_e in Eq. (2) – if we represent the time varying lift as the quantity represented in Eq. (1). Here, we will provide these comparisons to validate the numerical results.

In the present work, flow past a cylinder is solved first using a single-block structured grid, and then by using an overset grid. Same numerical methods are used for both the grids and any difference in performance will arise due to the method of solution in different sub-domains and the auxiliary boundary conditions at the sub-domain boundaries for the overset grid method. For the overset grid computations, we specifically report the role of interpolation errors by considering analytical test functions that mimic the vortices shed behind a cylinder.

One of the main purposes of this work is to extend the usage of high accuracy compact schemes [26,27] in solving complex geometry problems. Since these Padè schemes work on structured grids, one way they could be used for complex geometries is by using the overset grid methods [28,29]. This problem can also be tackled by other methods which use unstructured grids, or even by mesh-free least square-based methods [30]. The reason to use compact schemes arises due to their ability to resolve scales that is quite comparable to spectral methods, while avoiding the restrictions faced by the latter. Compact schemes are proposed here to solve flow past complex geometries or combinations of simple geometries with the computational domain multiply-connected. Most often, numerically generated grids do not have the desired properties and incur large error-degrading the quality of the results. This happens to be the case when the numerically generated grids are not orthogonal. In many reported cases in [27,31], compact schemes have been successfully used with orthogonal grids. It is possible to generate orthogonal, multiple, overlapping, block structured grids allowing one to use compact schemes in individual sub-domains. All compact schemes have been shown to suffer from numerical instability problem at one of the boundaries [26], and in the same reference it was avoided by using an optimum upwind compact scheme. Here, we have used one such optimum upwind compact scheme, OUCS3 to discretize convection and diffusion terms. Despite its relative success, there are problems of high levels of implicit filtering near the boundaries. Thus, it is mandatory to use over-lapped domains and invariably it is also used with non-coincident grid nodes in the overlap region of the sub-domains. This necessitates interpolation of data at the sub-domain boundaries from the data at the neighboring sub-domains for the inter-leaved calculation procedures [28,29]. In [28], authors report problems of interpolation, as a 10th order filter was required "to remove spurious waves generated by grid non-uniformities, boundary conditions and flow nonlinearities". In [29], the authors noted "that the interpolation generates spurious modes that depend on the wavenumbers of the signal" in the solution procedure for computational aero-acoustics problem. Thus, it is seen that the process of interpolation is a major factor in determining success of overset grid methods. In both these works [28,29], Lagrange interpolation has been used. To retain fourth order accuracy, it was necessary to take twenty-five points to interpolate the function values. There are other possibilities for taking lesser number of points for interpolation. For example, Ding et al. [30] have used a mesh-free least square-based finite difference method for numerical simulation of flows around two circular cylinders. In the present work, we compare Lagrange interpolation method with least square-based method in interpolating an analytical test function that mimics convecting vortices.

In [32], Landau equation was used computationally to study the cylinder wake in transient and post-transient stage. Also, POD was used to obtain a reduced order model to study the flow with varying Reynolds number. In the present study also the numerical methods have been evaluated by performing POD studies on simulation results obtained by these methods.

The paper is formatted in the following manner. In the next section, we present results of solving the Navier–Stokes equation for flow past a cylinder by representative methods in a single-block structured grid. In Section 3, effects of interpolation error is investigated for the Lagrange and the least square-based methods for a test function. This section also contains results obtained by solving Navier–Stokes equation for the same problem in an overset grid. In Section 4, we compare the POD of the data obtained by the single-block structured grid and by the overset grid methods and comment about the difference between the modes obtained using energy and enstrophy as the basis. In Section 5, we also show the application of overset method for flow past two cylinders in a side-by-side arrangement. Finally, summary and closing remarks are provided in Section 6.

2. Numerical simulation of vortex shedding

To compute flow past a circular cylinder, governing Navier–Stokes equations are represented in the stream function-vorticity ($\psi - \omega$) formulation. This formulation requiring fewer unknowns, allows higher resolution of the problem. Moreover, it also satisfies mass conservation exactly and presents no problems of pressure–velocity coupling, as the kinetics (vorticity transport equation or VTE) and kinematics (stream function equation or SFE) of the problem are decoupled. We solve the pressure-Poisson equation additionally to calculate loads and moment at any required time-instant using the calculated values of ψ and ω in an off-line mode.

Here, a computational domain is created analytically, where ξ is the azimuthal direction and η is along the radial direction. SFE and VTE are given, respectively, in the computational domain by,

$$\frac{\partial}{\partial \xi}\left(\frac{h_2}{h_1}\frac{\partial \psi}{\partial \xi}\right) + \frac{\partial}{\partial \eta}\left(\frac{h_1}{h_2}\frac{\partial \psi}{\partial \eta}\right) = -h_1 h_2 \omega \tag{3}$$

and

$$h_1 h_2 \frac{\partial \omega}{\partial t} + h_2 u \frac{\partial \omega}{\partial \xi} + h_1 v \frac{\partial \omega}{\partial \eta} = \frac{1}{Re}\left[\frac{\partial}{\partial \xi}\left(\frac{h_2}{h_1}\frac{\partial \omega}{\partial \xi}\right) + \frac{\partial}{\partial \eta}\left(\frac{h_1}{h_2}\frac{\partial \omega}{\partial \eta}\right)\right], \tag{4}$$

where h_1 and h_2 are the scale factors of the transformation given by,

$$h_1 = (x_\xi^2 + y_\xi^2)^{1/2} \quad \text{and} \quad h_2 = (x_\eta^2 + y_\eta^2)^{1/2}$$

with Greek subscripts indicating partial derivatives with respect to the corresponding transformed coordinates. The contra-variant components of velocity in the transformed plane are defined by,

$$h_2 u = \frac{\partial \psi}{\partial \eta} \quad \text{and} \quad h_1 v = -\frac{\partial \psi}{\partial \xi}. \tag{5}$$

All the equations reported here are in non-dimensional units, with the diameter (D) of the cylinder as the length scale, oncoming flow velocity U_∞ as the velocity scale and time is non-dimensionalized by D/U_∞. Thus, the Reynolds number appearing in (4) is given by, $Re = \frac{U_\infty D}{\nu}$, with ν as the kinematic viscosity.

Pressure is obtained numerically by solving the governing Poisson equation for the total pressure (p_t), given in an orthogonal coordinate system by [27,31,33],

$$\frac{\partial}{\partial \xi}\left(\frac{h_2}{h_1}\frac{\partial p_t}{\partial \xi}\right) + \frac{\partial}{\partial \eta}\left(\frac{h_1}{h_2}\frac{\partial p_t}{\partial \eta}\right) = \frac{\partial}{\partial \xi}(h_2 v \omega) - \frac{\partial}{\partial \eta}(h_1 u \omega), \tag{6}$$

where p_t is the total pressure and the SFE, as given in the self-adjoint form is discretized using second order central differencing scheme. Time integration is performed by the fourth order, four-stage Runge–Kutta (RK$_4$)-scheme. The nonlinear convection terms are discretized by the OUCS3-scheme for all the calculations here-as its ability in solving this particular flow has already been demonstrated in [23,33].

In discretizing the diffusion terms in (4), we note that the resolution of first and second derivatives numerically are quite different at high wave numbers, with the former filtering unknown completely at the Nyquist limit, $k\Delta x = \pi$. As compared to the first derivative discretization (irrespective of the method used), second derivative discretization does not completely filter the unknown at high wavenumbers. Even the second order central differencing (CD_2) does not attenuate the signal severely at high wavenumbers and at the Nyquist limit, second derivative is attenuated by $4/\pi^2$ times the actual value-as seen in the scaled wavenumber plane in Fig. 1 that is explained and discussed later. In contrast, if compact scheme for first derivative is used twice to calculate the second derivative, the computed quantities will be completely attenuated at the Nyquist limit. However, for the intermediate high wavenumbers the compact schemes can still outperform the CD_2 scheme. The Laplacian operators have been discretized by using either the CD_2 scheme or by applying OUCS3 scheme for first derivative [26,31] twice in Eq. (4), while CD_2 scheme has been used in Eqs. (3) and (6).
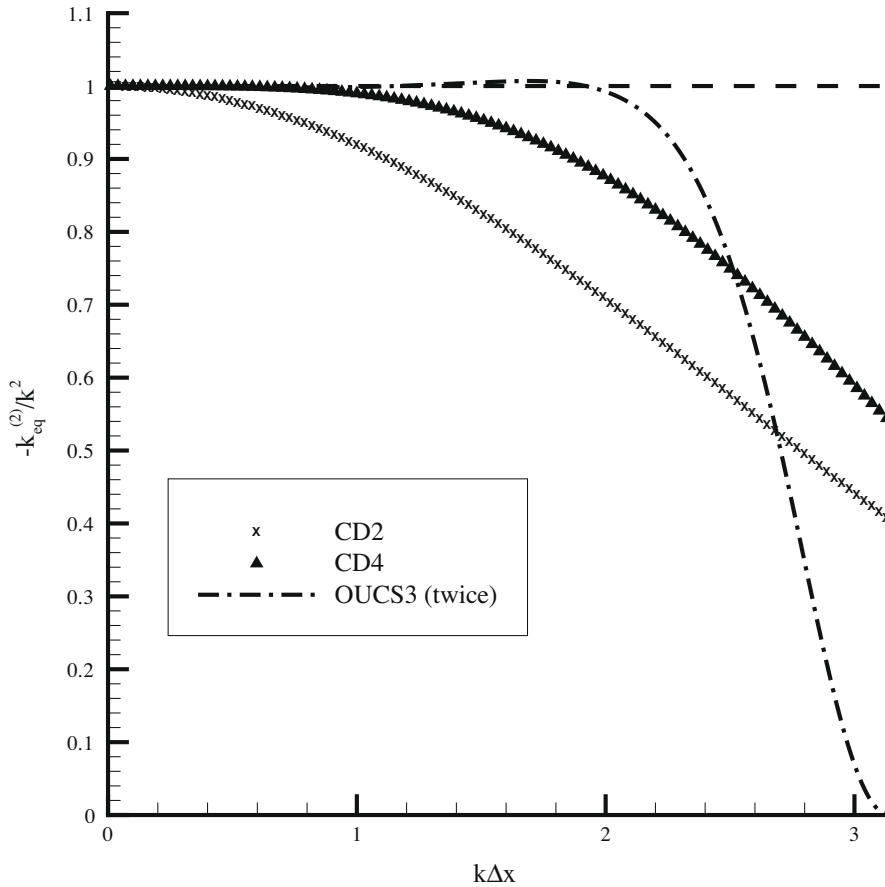

Fig. 1. Normalized effectiveness of dissipation discretization term using CD_2, CD_4 and OUCS3 scheme for first derivative twice shown as a function of scaled wavenumber.

If a function u is defined by its Fourier–Laplace transform via $u(x) = \int U(k)e^{ikx}dk$, then the exact first spatial derivative of u is given by $[\frac{\partial u}{\partial x}]_{exact} = \int ikUe^{ikx}dk$. Discrete computing methods obtain this first spatial derivative u' as $[u'_j]_{numerical} = \int ik_{eq}Ue^{ikx_j}dk$ with different methods having different expressions for k_{eq}. The quantity $\frac{k_{eq}}{k}$ is in general complex, with the real part representing the numerical method's ability to resolve various scales in the spectrum and the imaginary part adds numerical dissipation, when it is negative. One can adopt the same procedure in expressing the second spatial derivative in the spectral plane in a non-dimensional form, with the real part of $-\frac{k_{eq}^{(2)}}{k^2}$ representing scale-wise dissipation and the imaginary part representing added numerical dispersion.

In shorthand notation (using linear algebraic equation) one can write the second derivative in the physical plane as,

$$\{u'\} = \frac{1}{\Delta x}[D_1]\{u\}, \tag{7}$$

$$\{u''\} = \frac{1}{\Delta x^2}[D_2]\{u\}, \tag{8}$$

where Δx is the uniform grid spacing used for the purpose of analysis only.

Thus, $\frac{k_{eq}}{k}$ and $\frac{k_{eq}^{(2)}}{k^2}$ for first and second derivatives are evaluated from Eqs. (7) and (8) as,

$$\left(\frac{k_{eq}}{k}\right)_j = \frac{1}{k\Delta x}\sum[D_{1_{jl}}][P_{lj}],$$

$$\left(\frac{k_{eq}^{(2)}}{k^2}\right)_j = \frac{1}{(k\Delta x)^2}\sum[D_{2_{jl}}][P_{lj}],$$

where j defines the node number and $[P_{lj}] = e^{i(l-j)k\Delta x}$ is the projection matrix that helps defining the derivatives locally, so that a comparison is possible directly with spectral method. While the discretization of first derivative has been extensively studied, see e.g. the spectral plane analysis in [26,27], limited results exist comparing different methods for the discretization of second derivative. In Fig. 1, we have compared $k_{eq}^{(2)}/k^2$ in evaluating second derivative by the three methods: (i) classical CD_2 scheme; (ii) fourth order central difference (CD_4) scheme and (iii) the OUCS3 scheme for the first derivative applied twice. It is clearly noted that the CD_2 scheme has low effectiveness in discretizing second derivative for any wavenumber component above $k\Delta x = 0.3$. This effectiveness increases with the use of CD_4 method for an enhanced wavenumber range of $k\Delta x = 1$. For both these central difference schemes, effectiveness progressively deteriorates with increasing wavenumber, with none of them losing complete effectiveness at the Nyquist limit. In contrast, OUCS3 scheme shows an interesting behavior, as it retains full effectiveness of discretization up to $k\Delta x \sim 2$. However after this value of $k\Delta x$, the effectiveness declines rapidly to zero at the Nyquist limit. We note that the loss of dissipation discretization for a flow simulation is equivalent to not only performing a calculation at higher equivalent Reynolds number, but also distorting the diffusion operator due to difference in property brought about by differences in effectiveness in different directions. In Section 2.2, we will compare the results of Navier–Stokes equation obtained by the two methods of dissipation discretization.

2.1. Boundary and initial conditions

No-slip boundary condition on the surface of the cylinder is satisfied via:

$$\left(\frac{\partial \psi}{\partial \eta}\right)_{body} = 0. \tag{9}$$

Additional boundary condition on the body is given by,

$$\psi = \text{constant.} \tag{10}$$

The condition in Eq. (10) is used to solve the SFE, while both the conditions (9) and (10) are used to evaluate the wall vorticity (ω_b) that provides the boundary condition for the VTE.

At the outer boundary, uniform flow conditions are applied at the inflow (i.e. a Dirichlet condition on ψ) and a convective or Sommerfeld boundary condition on radial velocity at the outflow. This type of differentiation between inflow and outflow is mandatory to simulate realistically the lift and drag. The Sommerfeld boundary condition at the outflow is given by [33],

$$\frac{\partial u_r}{\partial t} + u_c(t)\frac{\partial u_r}{\partial r} = 0, \tag{11}$$

where u_r is the radial component of velocity and $u_c(t)$ is the convection velocity at the outflow at time t, which is obtained from the radial component of velocity at the previous time step, i.e. $u_c(t) = u_r(t - \Delta t)$ [33]. The initial condition is given by an impulsive start of the cylinder in a fluid at rest. The vorticity on the cylinder is obtained by using the kinematic definition of vorticity as given by (3): $\omega_b = -\frac{1}{h_2^2}\frac{\partial^2 \psi}{\partial \eta^2}$ at $\eta = 0$.

While using a single-block structured grid, we have used O-grid with 153 or 253 points in the azimuthal direction, spaced at equi-angular intervals and 400 points in the radial direction, with a tangent hyperbolic distribution of points and spacing

at the wall is given by, $\Delta r_w = 0.001$. The outer boundary is placed at 20 from the surface of the cylinder. The non-dimensional time step employed in all the reported calculations is $\Delta t = 4 \times 10^{-5}$.

2.2. Effect of grid and dissipation discretization

To perform this exercise, we compute the flow past a cylinder for $Re = 100$, using two sets of grids, with different number of points in the azimuthal direction. The CD_2 discretization method for the second derivative in conjunction with OUCS3 method for the convection term discretization will henceforth be referred to as the CD_2–OUCS3 method and we will refer as the OUCS3–OUCS3 method, when OUCS3 scheme is used to discretize both the convection and the diffusion terms.

In Fig. 2, we have compared the time history of lift and drag coefficient variation for the shown combination of methods and grids. It is interesting to note following the impulsive start, the flow retains top-down symmetry and the lift is zero up to a certain time, beyond which the flow becomes temporally unstable that can be adequately explained by a linear global
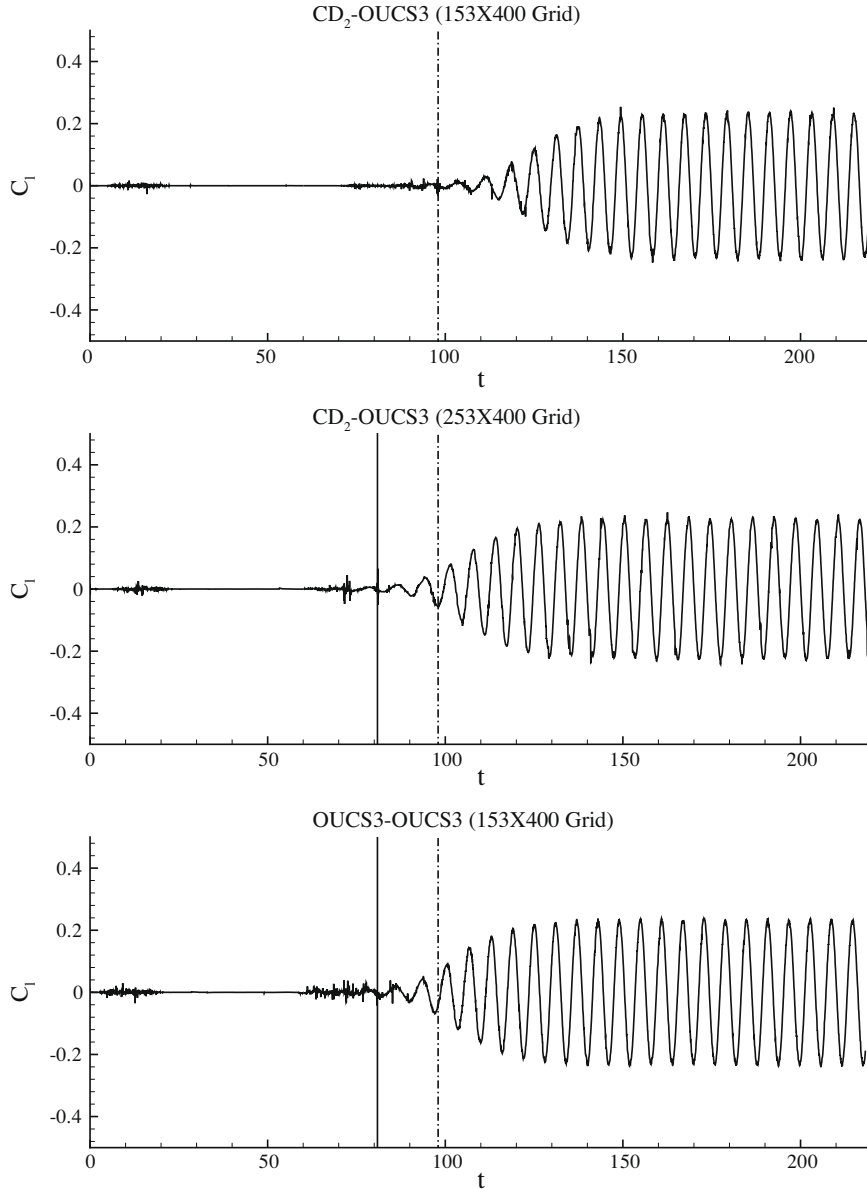

Fig. 2a. The time series of lift coefficient (C_l) obtained using single-block structured grid for $Re = 100$. On top, results obtained using CD_2–OUCS3 scheme with 153×400 grid; in the middle results obtained using 253×400 grid and at the bottom results obtained using OUCS3–OUCS3 method with 153×400 grid. The vertical dotted line indicates the onset of instability for the case shown on top and the vertical solid line indicates the onset of instability for the case shown in the middle.

framework [10–12,19,20,32]. This linearly unstable lift variation displays nonlinear saturation. It has been shown that this is a case of super-critical stability and can be very adequately explained by Landau model [8,9,19,20,32]. Thus, Fig. 2 displays the fact that once the flow transits from the steady state to a periodic limit cycle state following a linear instability and its nonlinear saturation, all methods and different grids employed here settle down to the same values of lift and drag coefficients eventually. This feature of the flow is characteristic of a hydrodynamic oscillator governed by the intrinsic dynamics of bluff body flow [34,35]. For such an oscillator, the system dynamics does not depend upon the background disturbance, which is also one of the features of the asymptotic solution as given by Eq. (2) for the Landau equation given by Eq. (1). Different grids or different numerical methods imply different background disturbance due to various sources of numerical error and Fig. 2 clearly establishes this aspect of the flow.

We also like to point out the differences between the simulation results using CD_2–OUCS3 method with 153 and 253 points in the azimuthal direction for the loads shown in Fig. 2. For the coarser grid, onset to vortex shedding occurs later as compared to the finer grid. To explain this behavior, let us note that the coarser grid filters higher values of k more
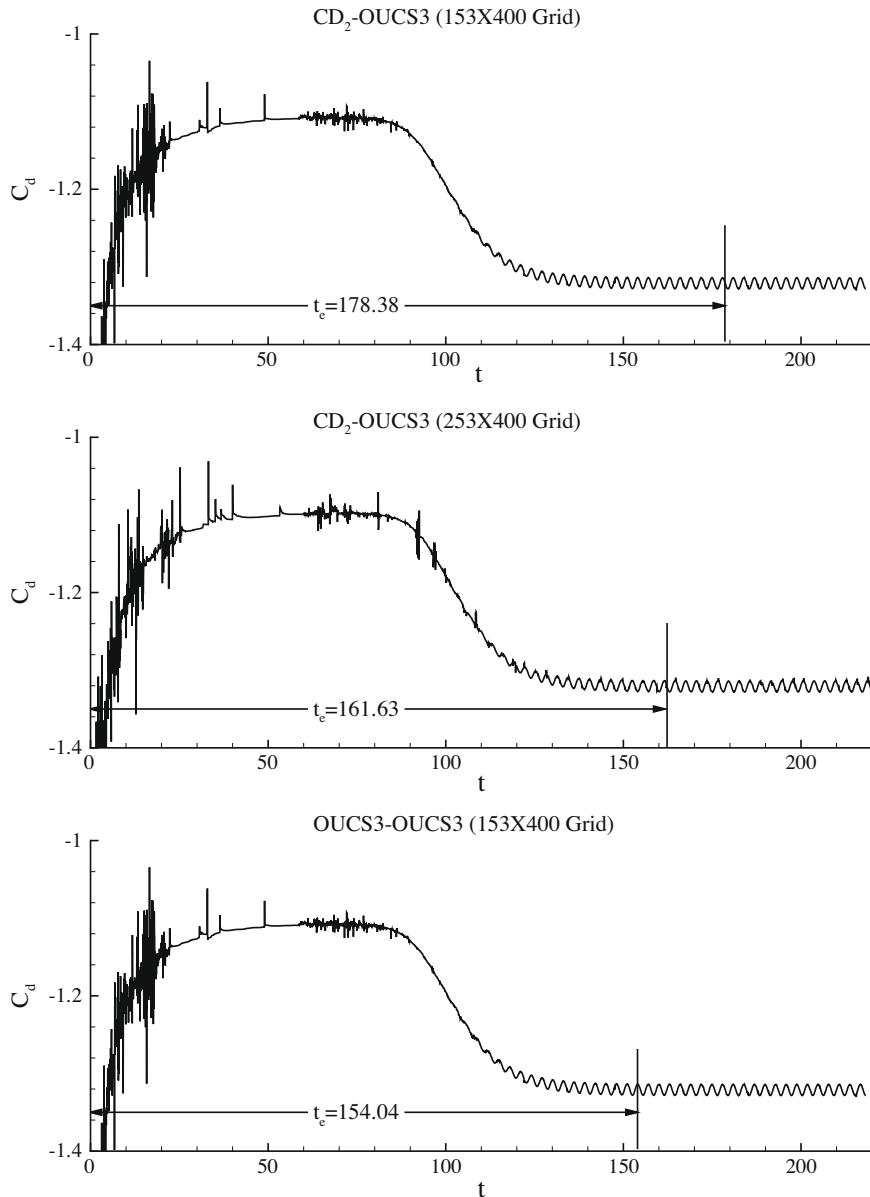

Fig. 2b. The time series of drag coefficient (C_d) obtained using single-block structured grid for $Re = 100$. On top, results obtained using CD_2-OUCS3 scheme with 153×400 grid; in the middle results obtained using 253×400 grid and at the bottom results obtained using OUCS3–OUCS3 method with 153×400 grid.

compared to the finer grid, in discretizing the convection term. Therefore, the coarser grid also displays lesser aliasing. One also notes that upon an impulsive start, the flow evolves with time as if the flow Reynolds number increases. Thus, as time progresses the propensity for aliasing increases with newer small length scales appearing in representing the convection terms. For this reason the flow simulated with finer grid gets affected at the Strouhal frequency by aliasing, earlier. This appears at small length scale that is shown in the lift variation in Fig. 2(a) as high frequency variation before the onset of asymmetry. This is due to the usage of higher order methods in discretizing convection terms. They would not be seen as readily for the lower order methods. We must also note that the discretization of diffusion terms have exactly the opposite effects as compared to the convection terms. A coarser grid exhibits larger loss of dissipation due to discretization whose effect is equivalent to increasing the effective Reynolds number. However, as the aliasing error arising out of discretization of convection terms overrides diffusion term effects, we notice earlier onset time for the finer grid. Furthermore, dissipation discretization by OUCS3 scheme brings in additional aliasing which is suppressed in the CD_2 method due to low-pass filtering by the latter. It is for this reason, OUCS3–OUCS3 method with (153×400) points displays even earlier onset time.

Landau, in his original paper, mentioned that the phase variation of lift and its rate cannot be ascertained definitively. There are various interpretations given in the literature [19,21,36] and we just mention in passing that concomitant to the amplitude equation given by (1), one can also write an equation for the phase rate (as given in [9,19,37]) that can be used to derive an amplitude dependent Strouhal number. From the simulation results shown in Fig. 2(a), one can obtain the Strouhal number and it is noted that this also remains the same irrespective of the method and the grid chosen. The compact scheme used has near-spectral accuracy and the number of points taken in the azimuthal direction is more than adequate to resolve the time scales in the flow. The only difference that is noted in the time variation calculated by different methods and grids is the onset time of the initial linear instability. This instability is related to the receptivity of the flow to different background disturbances. The time to reach equilibrium can be quantified by noting the time when the drag coefficient settles down to its time-average shown in Fig. 2(b)-as identified in the figure by different values of this time, t_e.

Computed vorticity contours obtained by CD_2–OUCS3 and OUCS3–OUCS3 are compared in Fig. 3, when the instantaneous lift attains maximum value in both the cases. The displayed results do not indicate any significant differences between the two frames. This is not surprising, as the dynamics is due to the oscillator-like behavior [35] whose time scale is large, i.e. the dynamics is governed by low frequency and the grid resolution required to capture this is very low and when the same grid is used for both the methods the dynamics is not affected by how the diffusion term is discretized. It is for this reason, rest of the computational results are provided using CD_2–OUCS3 method only-even for the overset grid method.

2.3. Validation of the numerical method

Used CD_2–OUCS3 numerical method for solving Navier–Stokes equation is validated next with various experimental and numerical results [24,25,30,38]. In Fig. 4, computed time-averaged drag coefficient at different low Re's are compared with the numerical results from [25] and experimental results from [38]. Numerical results have been obtained in [25] using an
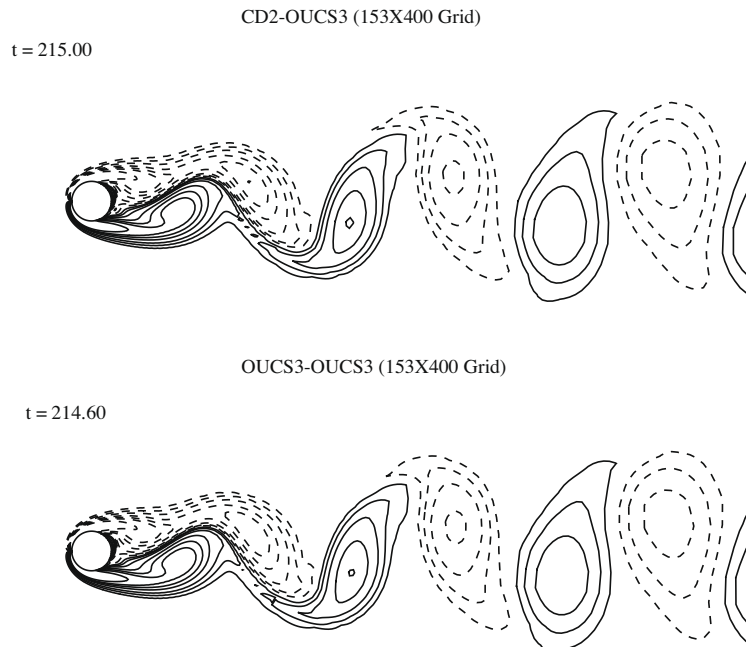

CD2-OUCS3 (153X400 Grid)

t = 215.00

OUCS3-OUCS3 (153X400 Grid)

t = 214.60

Fig. 3. Comparison of computed vorticity contours, by CD_2–OUCS3 scheme and OUCS3–OUCS3 method with 153×400 grid for $Re = 100$.
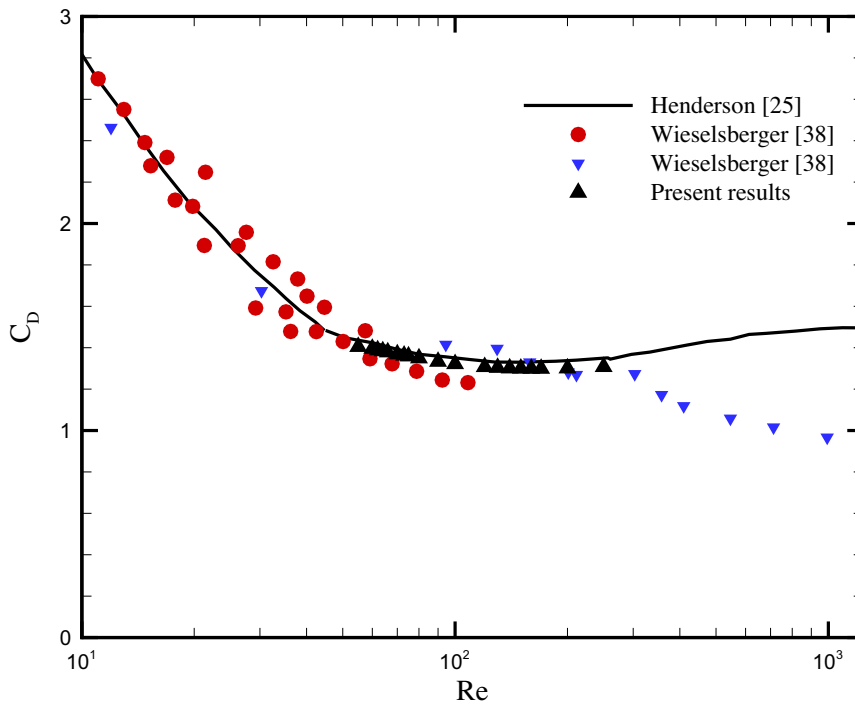
Fig. 4. Comparison of computed mean drag coefficient with experimental [38] and other computational results [25] using 153×400 single-block structured grid.

accurate spectral element method and the present computational results match excellently with these computations. Also the present computational results match very well with the experimental results given in Wieselsberger [38]. It is well known that the flow becomes three-dimensional for Re greater than about 250, as noted from the departure of the numerical results reported in [25] by 2D simulation from the experimental results of [38]. It is for this reason, we have not computed any case with higher Re than this limiting value.

In Fig. 5, variation of Strouhal number is shown with Reynolds number from the present computations. The computed values are compared with the numerical computations of [25] and the experimental results of [24,39]. Present computational results match quite well with the other three sets of results. It is noted that the Strouhal number obtained in [24] in a wind tunnel is for $Tu = 0.06\%$, while the computations are for uniform flow without any noise. Hence, a more valid comparison should be made with other accurate computations and it is noted that the present computations match with the computed results of [25]. We also note another aspect of the experimental results that these are essentially data-fits by single analytical functions. Hence they are empirical in nature and would not show variations shown in the present computations.

Validation of the present method is also provided by comparing the computed amplitude of asymptotic lift variation as a function of Reynolds number in Fig. 6. The computed equilibrium amplitude of the limit cycle matches quite well with the experimental correlation given in [24], once again verifying the correctness of the present numerical method (CD_2–OUCS3) using a single-block structured grid. Present calculations show critical Reynolds number that is 51.93 which is not too different from that shown in Fig. 14 of [20]. Having established the correctness of the method with the single-block structured grid, we will use these results to further validate the computations performed using overset grids.

3. Flow field calculation using overset or chimera grid technique

From the results shown in the previous section, one notes the CD_2–OUCS3 method to possess desired numerical properties in solving bluff body flow problems in capturing various linear instabilities and their nonlinear saturation using a single-block structured grid. As explained in the introduction, compact schemes are not amenable for use with flow past complex geometry unless some provision is made to represent such bodies with overset multiple-block structured grids. It is even better if orthogonal grids can be generated in different blocks with common overlapping zone through which information can propagate across the sub-domains. Keeping these in view, we employ overset grid technique employing different orthogonal grids in different sub-domains. For the problem of flow past a cylinder, a schematic overset grid system is shown in Fig. 7, where a polar grid around the circular cylinder (shown as Ω_2) is overset on a background Cartesian grid (Ω_1). Using a single-block structured O-grid around a circular cylinder, one requires solving the problem with many points upstream where the flow

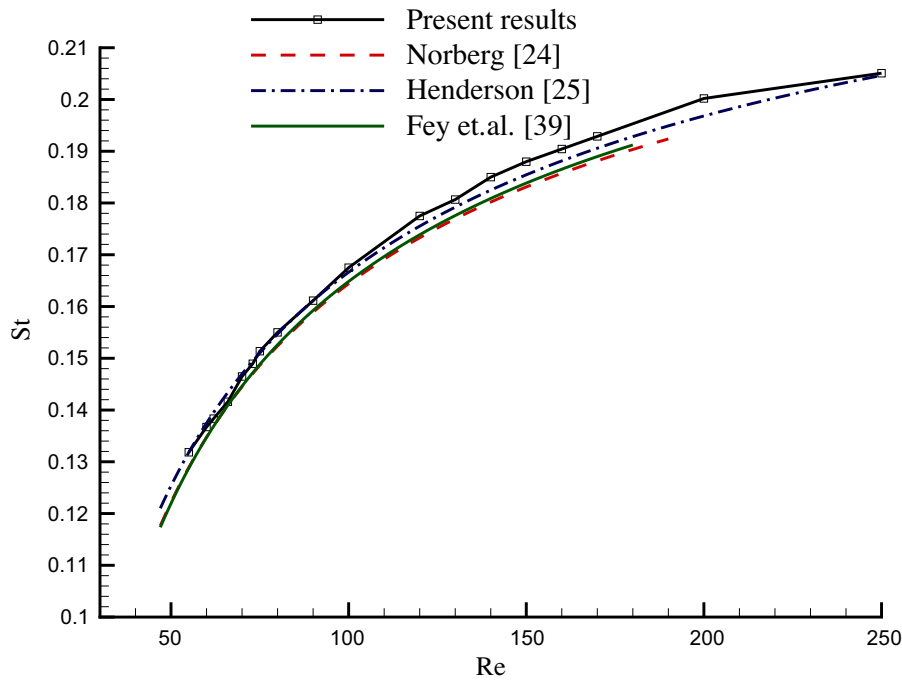**Fig. 5.** Comparison of computed Strouhal number with experimental [24,39] and other computational results [25] using 153×400 single-block structured grid.

does not change appreciably from its uniform condition. This can be avoided with overset grid methods, while one can resolve the wake more accurately by taking additional points in the wake part of the Cartesian grid. In a latter exercise, we will also show results for uniform flow past two cylinders kept in a side-by-side arrangement, as a further illustration of overset grid method's applicability along with the use of compact scheme.

As shown in the figure, the Cartesian grid (Ω_1) in the vertical direction is fine near the center of the domain that stretches following a tangent hyperbolic fashion [31] in the y-direction. For the Cartesian grid in the horizontal direction, stretching is
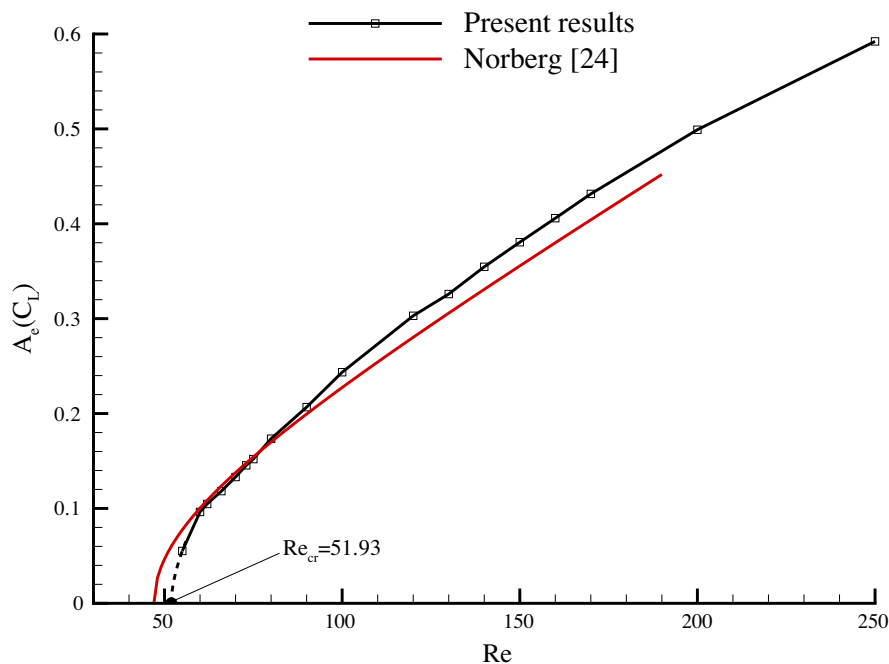

Fig. 6. Comparison of computed fluctuating lift coefficient amplitude with experimental [24] using 153×400 single-block structured grid.
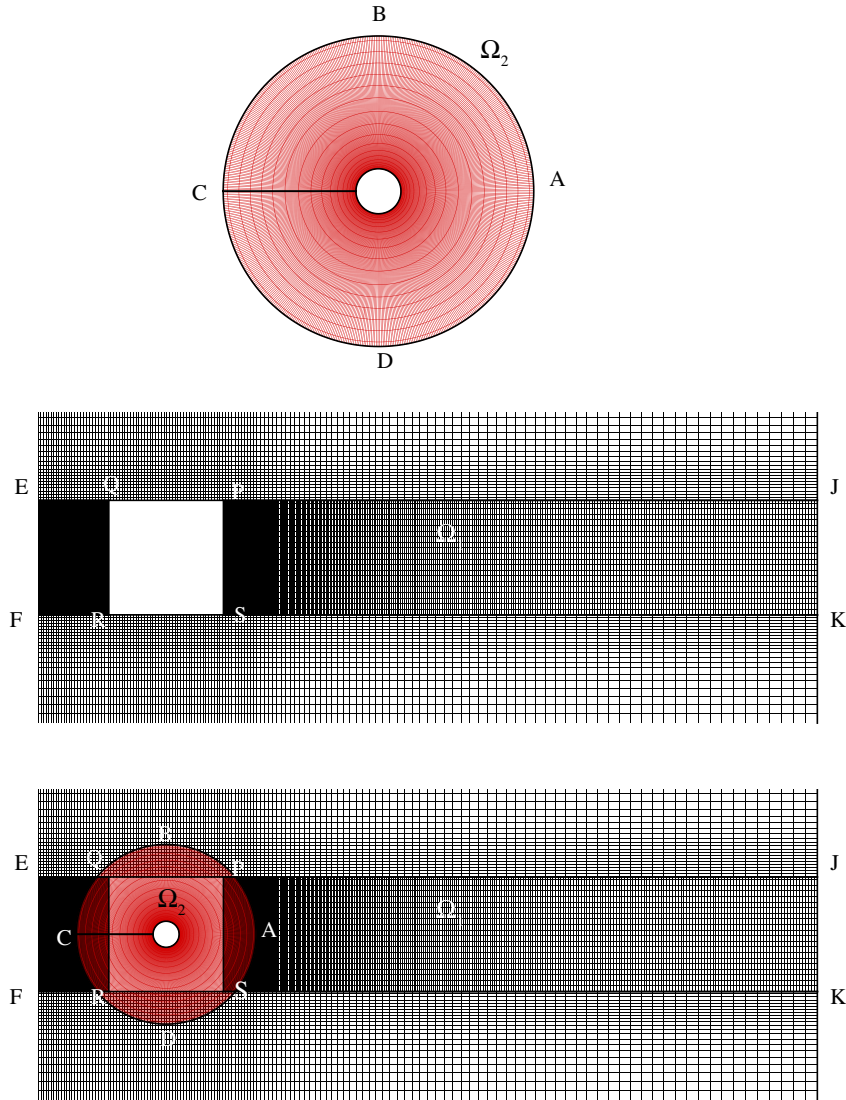
Fig. 7. Used overset grid for flow past a single cylinder. On top, the polar grid around the cylinder; in the middle the Cartesian grid with the cutout in the middle and at the bottom the composite grid is shown.

used as one moves away from the cylinder in the upstream and downstream direction following the similar tangent hyperbolic function with different stretching parameters. The grid in the radial direction for Ω_2 is stretched by similar hyperbolic tangent function starting from the cylinder outwards. It can be shown that such stretching allows one to reduce aliasing error [27].

Navier–Stokes equation is solved independently in each sub-domain, while communicating with neighboring sub-domains through the exchange of auxiliary boundary conditions those created by interpolation of variables from a set of *donor grid-points* to the *recipient grid-points*. For example in Fig. 7, variables on the inter-grid boundary PQRS of domain Ω_1 are obtained from solutions in Ω_2. In a similar way, boundary condition on inter-grid boundary ABCD is obtained from the neighboring domain Ω_1. This interpolation at the inter-grid boundaries plays a major role in performing overset grid computations accurately. In [28,29], a bi-directional Lagrange interpolation technique is used for this interpolation, that requires information from 25 *donor points* for each *recipient point*. Here, we compare this interpolation strategy with the weighted least squares interpolation used in [30]. In both these strategies, once a *recipient point* is identified, the nearest grid point from the *donor grid* is located by a directional search algorithm [40].

In Lagrange interpolation technique, with respect to the nearest grid point of the *recipient point*, we take a patch of points extending in both the ξ- and η-directions, enabling a finite order polynomial fit of the function. Here, the interpolating function is obtained from,

$$f(\xi,\eta) = \sum_{i=1}^{N} \sum_{j=1}^{M} f(\xi_i, \eta_j) l_i(\xi) m_j(\eta), \tag{12}$$

where $l_i(\xi)$ and $m_j(\eta)$ are the Lagrange polynomials with specific form [41] shown for the *i*th member of $l(\xi)$ as,

$$l_i(\xi) = \prod_{\substack{j=1 \\ j \neq i}}^{N} \frac{\xi - \xi_j}{\xi_i - \xi_j}. \tag{13}$$

These polynomials have the desired property: $l_i(\xi_j) = \delta_{ij}$, with δ_{ij} as the Dirac delta function. The interpolation procedure is explained here with the help of Fig. 8. After locating the nearest point '1' in Ω_1 for the *recipient point* P in Ω_2, we locate two additional sets of points in all directions of '1'. This makes a cloud of 25 points (identified by the dotted rectangle in the figure, including the nearest point '1'), those are used for the fourth order Lagrange polynomial. Similarly, for the *recipient point* Q in Ω_1, we identify the cloud of 25 points in Ω_2-shown by the dashed trapezoid in the figure around the nearest point '1'.

The Lagrange interpolation technique given by Eq. (12), is compared next with a Taylor series based method whose description is given in [42]. For this interpolation, a variable is expressed in terms of a Taylor series for the 2D problem as,

$$f(\xi, \eta) = f(\xi_0, \eta_0) + \frac{\partial f}{\partial \xi}(\xi - \xi_0) + \frac{\partial f}{\partial \eta}(\eta - \eta_0) + \cdots, \tag{14}$$

where the quantities with subscript 0 refer to the *recipient point* and the above relation can be used successively at the *donor points* by identifying their coordinates (ξ, η). Minimum number of donor points needed, fixes the order of interpolation. For example, for linear interpolation, Eq. (14) is satisfied at three points to obtain f and the two first derivatives at (ξ_0, η_0). In [43], it was suggested to satisfy Eq. (14) at more than the required number of points in a least-square framework to achieve higher accuracy. Apart from interpolating the function by the least-square approach in this interpolation method as compared to the Lagrange method, second difference stems from the different weights given in these two methods at the donor grid points.

There are two aspects of interpolation while solving flow over bluff bodies: (i) firstly, passage of vortices or disturbance fronts from one sub-domain to another can incur errors due to interpolation. This is the scenario in all vortex-dominated flows and (ii) secondly, even when such vortices are not present, interpolation error can be a significant source of numerical disturbance that can alter or trigger flow instabilities. Both these aspects are investigated in the following section with the help of an analytical test function.

In order to assess interpolation schemes properly, a function is carefully chosen that has rapid variations, as in fluid flow problem displaying passage of vortices through the sub-domain boundaries. Any simple function can be interpolated easily up to 10 decimal place accuracy by both the Lagrangian and Taylor series based procedures-using lowest order interpolation
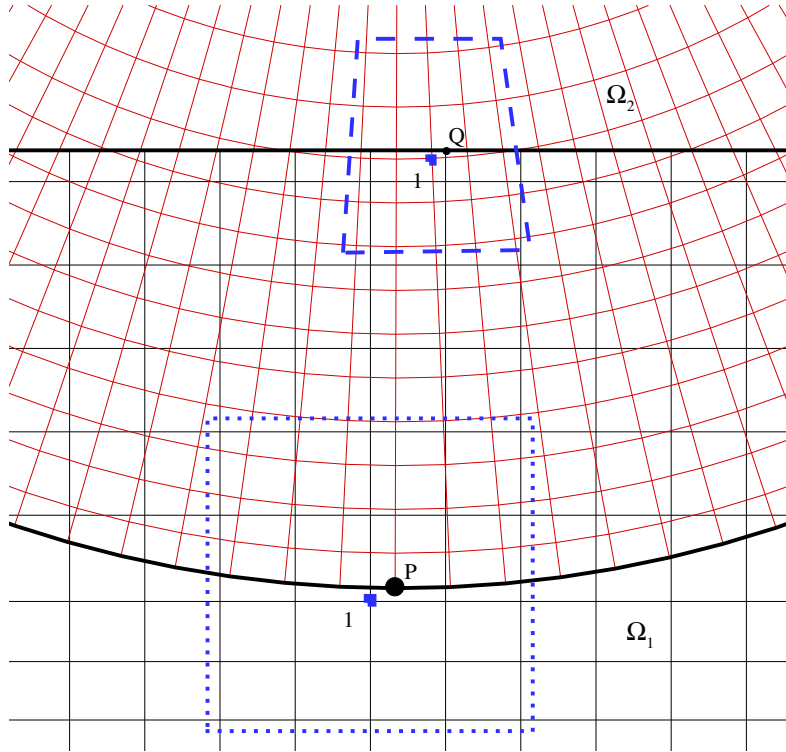

Fig. 8. Used overset grid near the sub-domain boundary for flow past a single cylinder. For the boundary condition in the polar grid at P, we have identified the donor grid points within the dotted square; for the boundary condition in the Cartesian grid at the recipient point Q, the donor points are similarly identified within the dashed box.

[40]. However, passage of vortical structures act like moving fronts, that should be resolved successfully with the interpolation scheme for overset grid method.

Such a function chosen here is given by,

$$g(x, y) = A_1 e^{-\alpha[(x-x_0)^2 + (y-y_0)^2]} \tag{15}$$

with $A_1 = 100$; and $x_0 = 3.0$, $y_0 = 3.7$ (with the origin fixed at the center of the cylinder) to interpolate the function on the periphery of Ω_2, on which P is a member, as shown in Fig. 8. For the present study a (150×150)-grid in Ω_2 (in the polar grid stretching up to five D) and a (580×735)-grid in Ω_1 (in the domain $-7.5 \leqslant x \leqslant 25$; $-12 \leqslant y \leqslant +12$) sub-domains are used. The function in Eq. (15), puts a different demand on the interpolation function, depending upon the value of α. A lower value of α represents a diffused structure, while increased value implies a structure that is very sharp and coherent. While the structure simulates a circular vortex patch, one can supply different shapes to the front as well. However, we restrict ourselves to a circular front only.

In a least-square Taylor series interpolation framework, a two-dimensional function $g(\mathbf{x})$ and its derivatives $\partial g_{N1X1}[= (1, \partial_x, \partial_y, \partial_x^2, \partial_x\partial_y, \ldots, \partial_y^n)^T g]$ defined at $\mathbf{x} = (x_0, y_0)$ are given by

$$g_{N1X1} = [F]_{N1XN1} \partial g_{N1X1}, \tag{16}$$

where $N = n(n+1)/2$; $N1 = N + 1$; $g_{N1X1} = (g_1, g_2, \ldots, g_{N1})^T$ and the matrix $[F]$ is given by,

$$[F] = \begin{pmatrix}
1 & \Delta x_1 & \Delta y_1 & \Delta x_1^2/2 & \Delta x_1 \Delta y_1 & \Delta y_1^2 & \ldots & \Delta y_1^n/n! \\
1 & \Delta x_2 & \Delta y_2 & \Delta x_2^2/2 & \Delta x_2 \Delta y_2 & \Delta y_2^2 & \ldots & \Delta y_2^n/n! \\
1 & \Delta x_3 & \Delta y_3 & \Delta x_3^2/2 & \Delta x_3 \Delta y_3 & \Delta y_3^2 & \ldots & \Delta y_3^n/n! \\
\vdots & \ldots & \ldots & \ldots & \ldots & \ldots & & \vdots \\
\vdots & \ldots & \ldots & \ldots & \ldots & \ldots & & \vdots \\
\vdots & \ldots & \ldots & \ldots & \ldots & \ldots & & \vdots \\
\vdots & \ldots & \ldots & \ldots & \ldots & \ldots & & \vdots \\
\vdots & \ldots & \ldots & \ddots & \ldots & \ldots & & \vdots \\
1 & \Delta x_{N1} & \Delta y_{N1} & \frac{\Delta x_{N1}^2}{2} & \Delta x_{N1}\Delta y_{N1} & \Delta y_{N1}^2 & \ldots & \frac{\Delta y_{N1}^n}{n!}
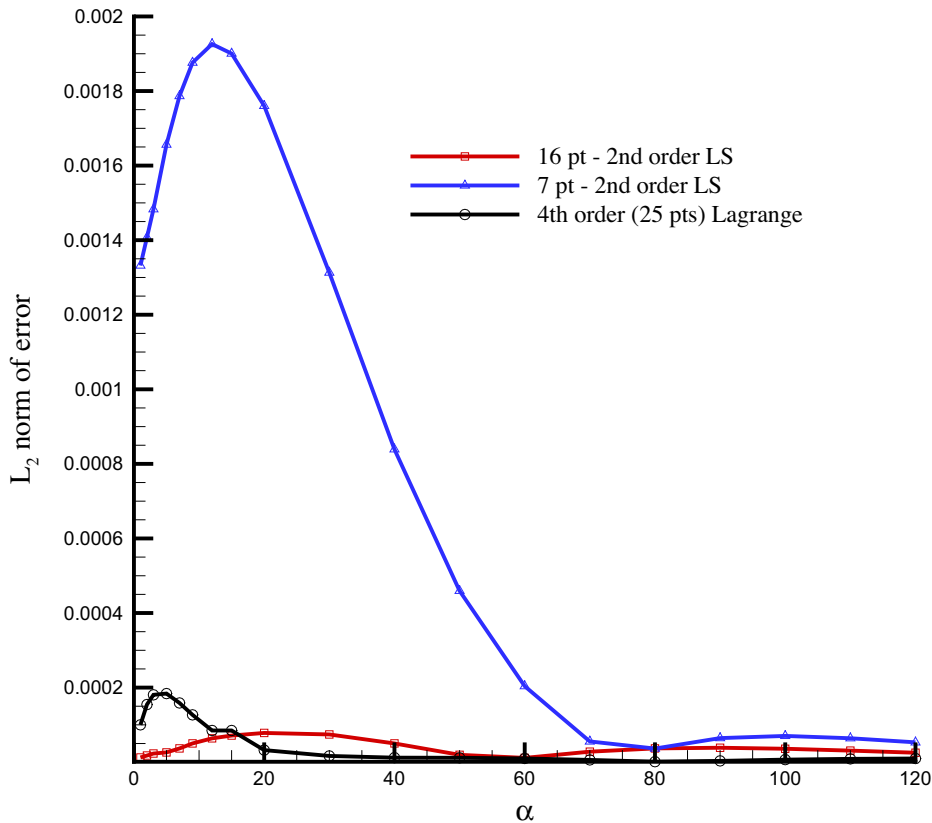\end{pmatrix}.$$

Fig. 9. L_2-norm of error for the interpolation of the analytic function (Eq. (15)) plotted as a function of the parameter α. Here, the error for second order least square methods with 7- and 16-points are compared with the fourth order Lagrange interpolation method that requires 25 donor points.

Following the weighted least square formulation of [42], the function and derivative at the recipient point are obtained from:

$$\partial g = ([F^T][W][F])^{-1}[F^T][W]g, \tag{17}$$

where $[W] = Diag\{w_1, w_2, w_3, \ldots, w_{N1}\}$ is the diagonal matrix of the weight factor, whose individual entry is given by $w_i = \sqrt{4\pi^{-1}}(1 - |\Delta x_i/d_0|^2)^4$. Distance between the maximum distant point and the recipient determines d_0 in the weight functions. In the present work, we have tested for the second and third order least square formulations and compared them with the fourth order Lagrange interpolation.

To estimate the efficiency of interpolation, we sum up the error created by the estimated values with respect to the exact values given by Eq. (15), on the outer boundary of Ω_2, for both the interpolation strategies. In Fig. 9, we have compared this error norm (L_2-norm) for the fourth order Lagrange interpolation results with second order least-square interpolation scheme (with six unknowns) with different number of *donor points* for different values of α. It is clearly evident that for the second order least square interpolation with 7-points error is significantly more, as compared to the case of using 16-points for low to moderate values of α. The choice of 7-points imply adding only one extra point to what is needed for uniquely determining ∂g. Choice of 16-points was made after preliminary studies with 9-, 16- and 25-points revealed that 16-points produced minimum error. When we compare the 4th order Lagrange interpolation scheme with the 16-points least square results, we notice an interesting aspect. For low values of α (less than 15), 16-point least square method performs better than the fourth order Lagrange interpolation scheme. However, for large values of α, i.e. when the test function represents a sharper variation, the Lagrange interpolation performs better. In contrast, for a diffused front (characterized by low value of α) the least square interpolation with 16-points performs better.

To understand the role of order of interpolation for the least square method better, in Fig. 10, we have compared second and third order 16-points least square schemes. Once again one notices that the higher order scheme performs poorly for lower values of α. However, at higher values of α, both the schemes display almost similar properties. Obviously, the higher order method requires more number of partial derivative evaluations and therefore more computational effort at each step of time advancement of the solution procedure.

The L_2-norm shown in the previous two figures show integrated properties. To further understand the distribution of error along the periphery of Ω_2, in Fig. 11, we have compared the error distribution as a function of the azimuthal grid index for
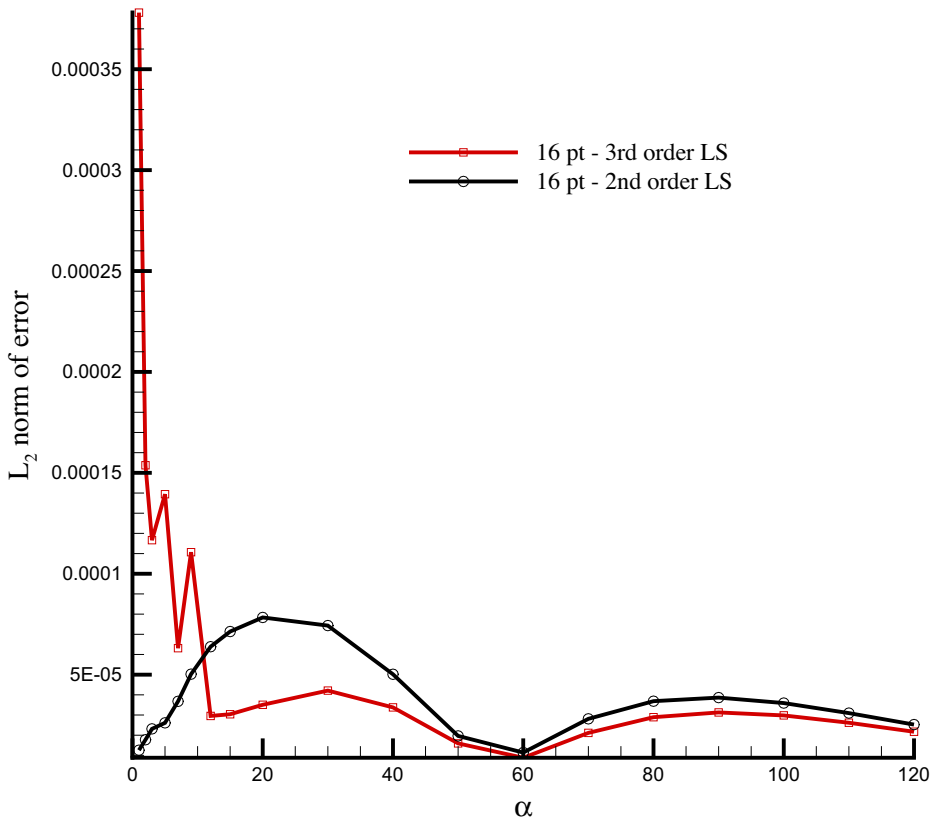

Fig. 10. L_2-norm of error for the interpolation of the analytic function (Eq. (15)) plotted as a function of the parameter α for second and third order least square methods with 16 points.
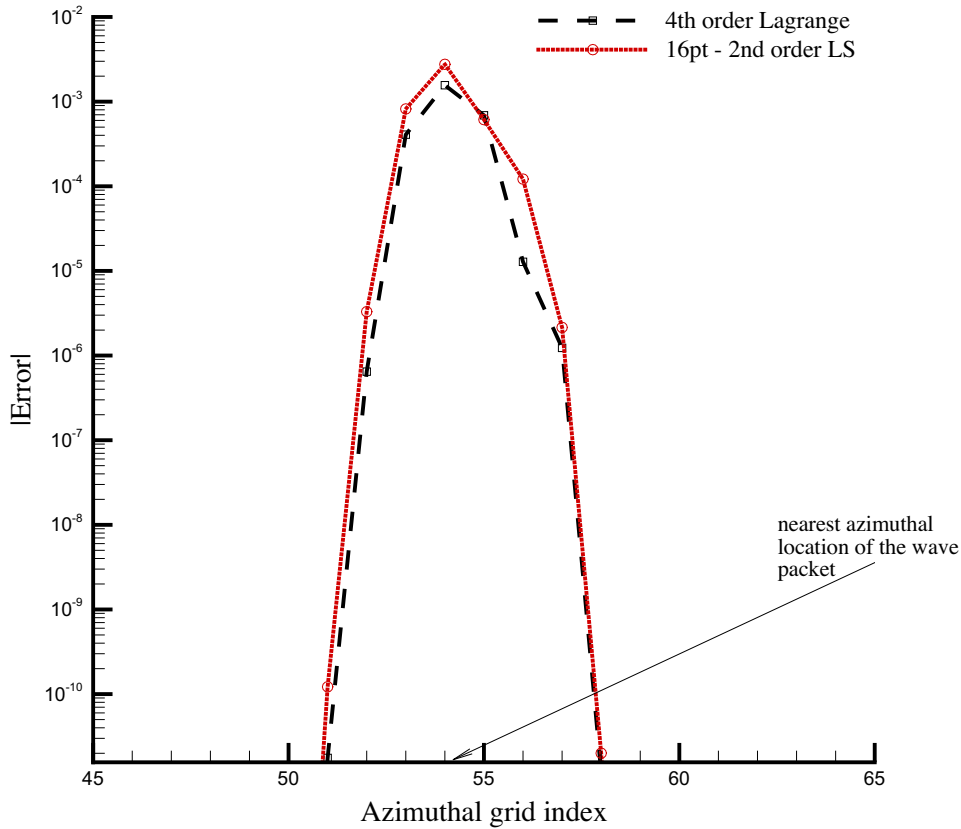
Fig. 11. Error for the interpolation of the analytical function (Eq. (15)) plotted as a function of azimuthal location on the boundary of Ω_2 compared between the second order least square method with fourth order Lagrange interpolation scheme.

the Lagrange interpolation and the 16-points second order least square scheme for $\alpha = 50$. In the figure, we have also marked the location of the point on the outer boundary of Ω_2 that is nearest to the core of the structure given by the point (x_0, y_0) in Eq. (15). It is evident that a larger contribution to the L_2-norm for the Lagrange interpolation comes from very few selective points near (x_0, y_0). Corresponding contribution of error in the least squares scheme comes from more number of points. Based on these observations, for rest of the reported results we have used the fourth order Lagrange interpolation scheme.

Next, we report results using overset grid method for the solution of flow past circular cylinder at $Re = 100$. In this calculation, the sub-domain, Ω_1 is defined in $(-5 \leqslant x \leqslant 25; -12 \leqslant y \leqslant 12)$ with (581×427) grid points. Around the cylinder, a square cutout of size (4.4×4.4) is made. The polar sub-domain is given by the outer diameter of size 3.45 and in this domain, 550 uniformly distributed points have been taken in the azimuthal direction and 185 stretched points are taken in the radial direction. Pressure field is calculated in a part of Ω_2 whose outer boundary extended up to 2.07 only. Apart from calculating the loads in this truncated domain, POD is also performed using data in this domain.

In Fig. 12, vorticity contours have been compared between the cases of using a single-block structured grid and an overset grid as described above. The time frames are chosen within one full cycle, equi-spaced in phase as seen in real non-dimensional time. Same contours have been plotted in all the frames for the ease of comparison and one notes extremely close resemblance between these two sets of results for identical phase.

In the following table, we have compared the computed values of lift and drag coefficients and the Strouhal number by the present two methods and the results given in [30,44] for flow past a circular cylinder at $Re = 100$. It is readily evident that all the results for the fluctuating lift are close to each other. Fluctuating drag varies depending upon the additional sources of noise due to interpolation, as in the present overset grid case and that in [30]. However, the Strouhal number appears to remain very close to each other for all the displayed cases. These results could also be viewed as an extension of Section 2.3 where we have validated our single-block structured grid computations.

The overset grid method calculations produce a larger mean and fluctuating drag value, as compared to the single-block structured calculation by the presented method. Results obtained in [30] seems to over-predict lift and drag, although the Strouhal frequency is captured well. Thus, it is apparent that to compare numerical methods, comparing just the Strouhal number does not provide adequate basis to judge the suitability of a numerical method. It is much more important to look at the amplitudes of time varying quantities. Also, we have added the comparison of eigenfunctions obtained by POD for effective comparison of methods as discussed in the next section.

4. POD of results obtained using single-block structured and overset grid methods

Proper orthogonal decomposition is often used to characterize space–time dependent data, specifically if the data set is stochastic in nature. This happens to be the case for turbulent flows and in [45] this topic is dealt with in detail. The method of snapshots, as given originally in Sirovich [46] is used here. In [32] POD was used to study the transient and post-transient stages of wake development behind a single circular cylinder. In [33], POD of computational data was used to study control of vortex shedding behind circular cylinder. Thus, the usage of POD to study flow instability for bluff body flows is already well established. The method of snapshots is now a well known method to provide valuable insight into the eigenmodes of high degree of freedom dynamical systems and in the following, we use POD with the computed data from single-block structured and overset grid methods, to provide comparison between these two sets of eigenmodes. We have performed
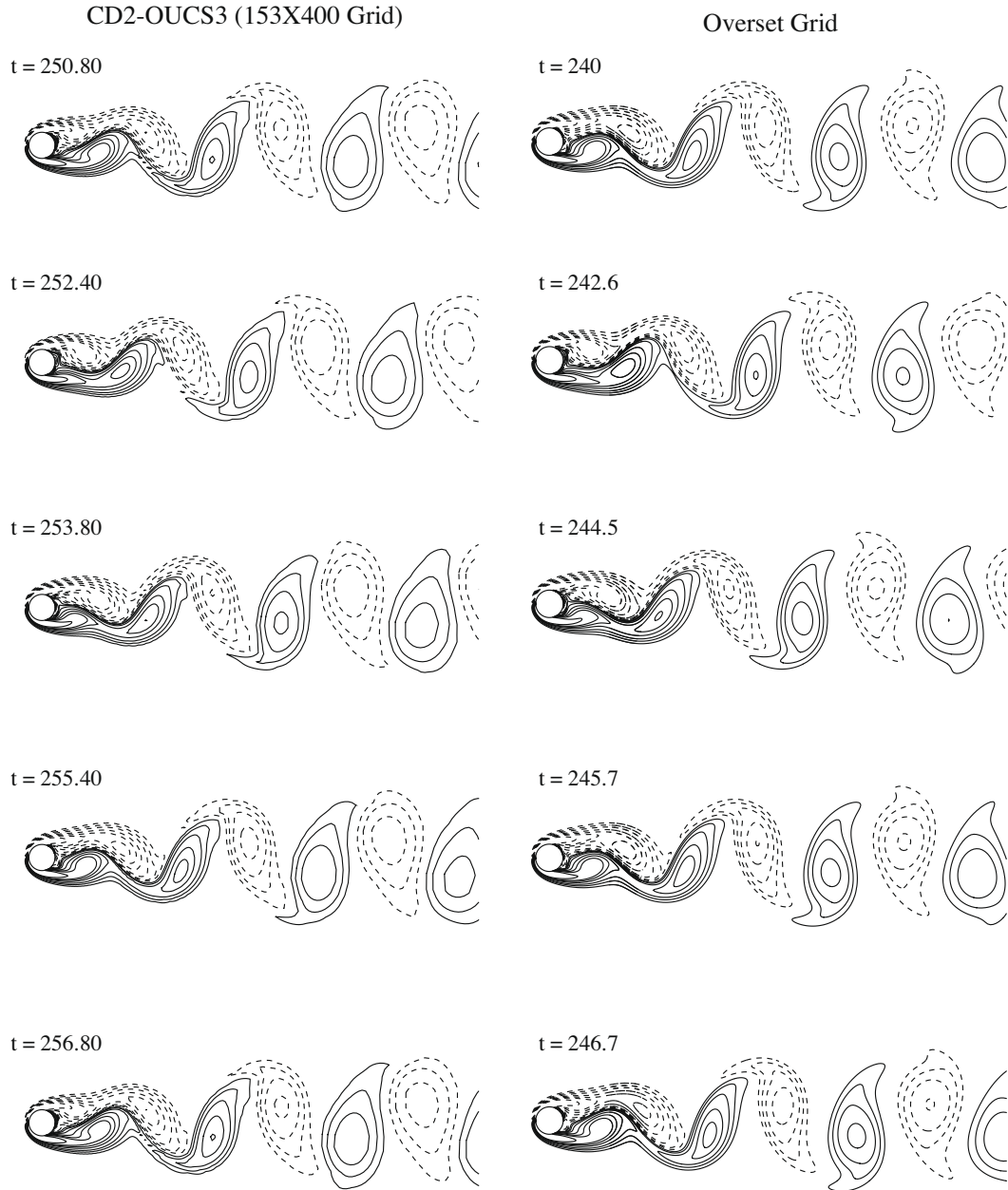

Fig. 12. Comparison of computed vorticity contours for single-block structured grid (left) and overset grid (right) for *Re* = 100 and the results are shown for one cycle.

the POD of the data in identical domain, that corresponds to a part of Ω_2 for the overset grid as defined in the previous section.

Vortical structures obtained from the POD analysis of vorticity data provide a statistical fit of the ensemble during the time period, by minimizing the projection error of the data onto a set of deterministic eigenvectors. The eigenvectors (X) are obtained from the linear algebraic equation: $RX = \lambda X$, with R as the covariance matrix whose elements are formed from
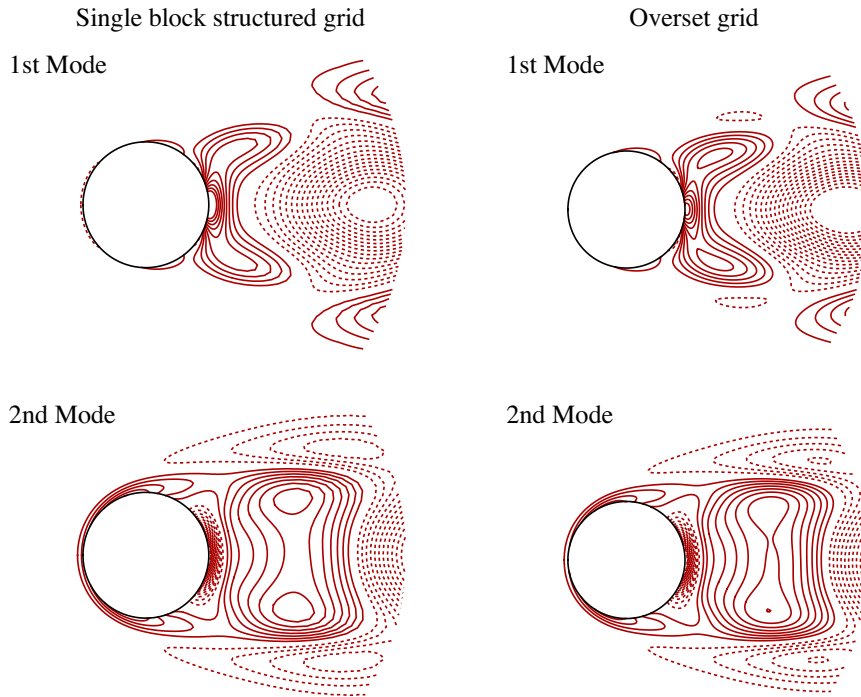

Fig. 13a. Comparison of the first two eigenmodes obtained by proper orthogonal decomposition (POD) for enstrophy for single-block structured (left) and overset grid (right) for $Re = 100$. The dataset is for one cycle of variation and the POD is obtained on a part-domain in Ω_2 for both the cases.
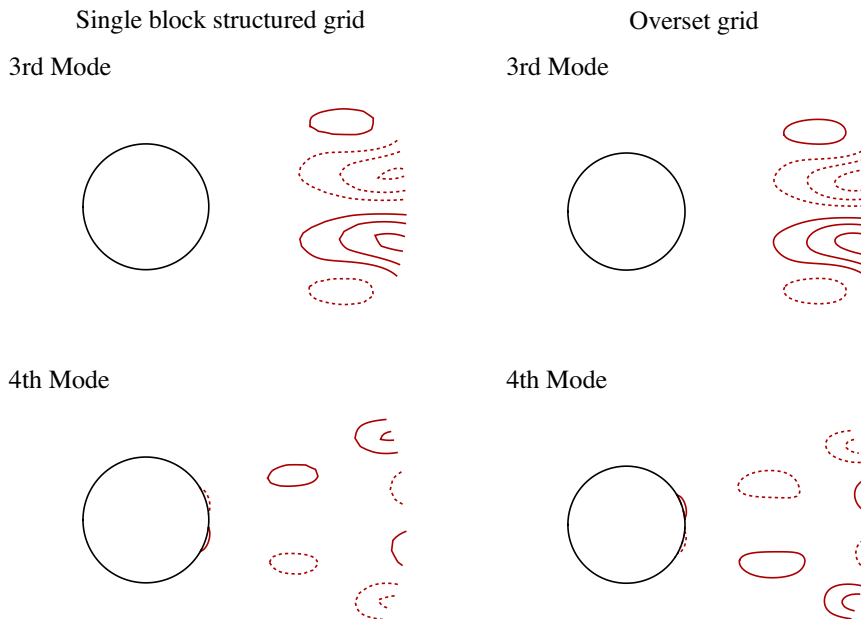

Fig. 13b. Comparison of the third and fourth eigenmodes obtained by proper orthogonal decomposition (POD) for enstrophy for single-block structured (left) and overset grid (right) for $Re = 100$. The dataset is for one cycle of variation and the POD is obtained on a part-domain in Ω_2 for both the cases.

the disturbance vorticity ($\omega(x_i, t_m)$) as: $R_{ij} = 1/M\sum_{m=1}^{M}\omega'(x_i,t_m)\omega'(x_i,t_m)$, with $i,j = 1, 2, \ldots, N$ defined over all collocation points totaling to N. These complete eigenvectors correspond to the eigenvalues λ that define the probability of their occurrence and their sum gives the total enstrophy of the system for the vorticity data.

In flow past a cylinder at low Reynolds numbers, the Strouhal number defines the largest and the most important time scale. Additionally, there can be higher frequency events present in the flow. Thus, in applying the POD, we apply method of snapshots with data taken from one peak to another in the time series of lift data. First, we use the vorticity data and perform POD for enstrophy. In Fig. 13(a), we have shown the first two eigenmodes for the single-block structured and the overset grid data. In these figures, the value spans from −8.0 to 4.5 and we have drawn contours at an interval of 0.5, excepting the zero contour. It is clearly evident from the eigenvalues that the first four modes are more than adequate to characterize this flow. In Fig. 13(b), third and fourth eigenmodes are shown and one notices very marginal differences between the two sets of POD. For example, in the first mode an additional contour of value −0.5 is seen in the overset grid data in the near wake.
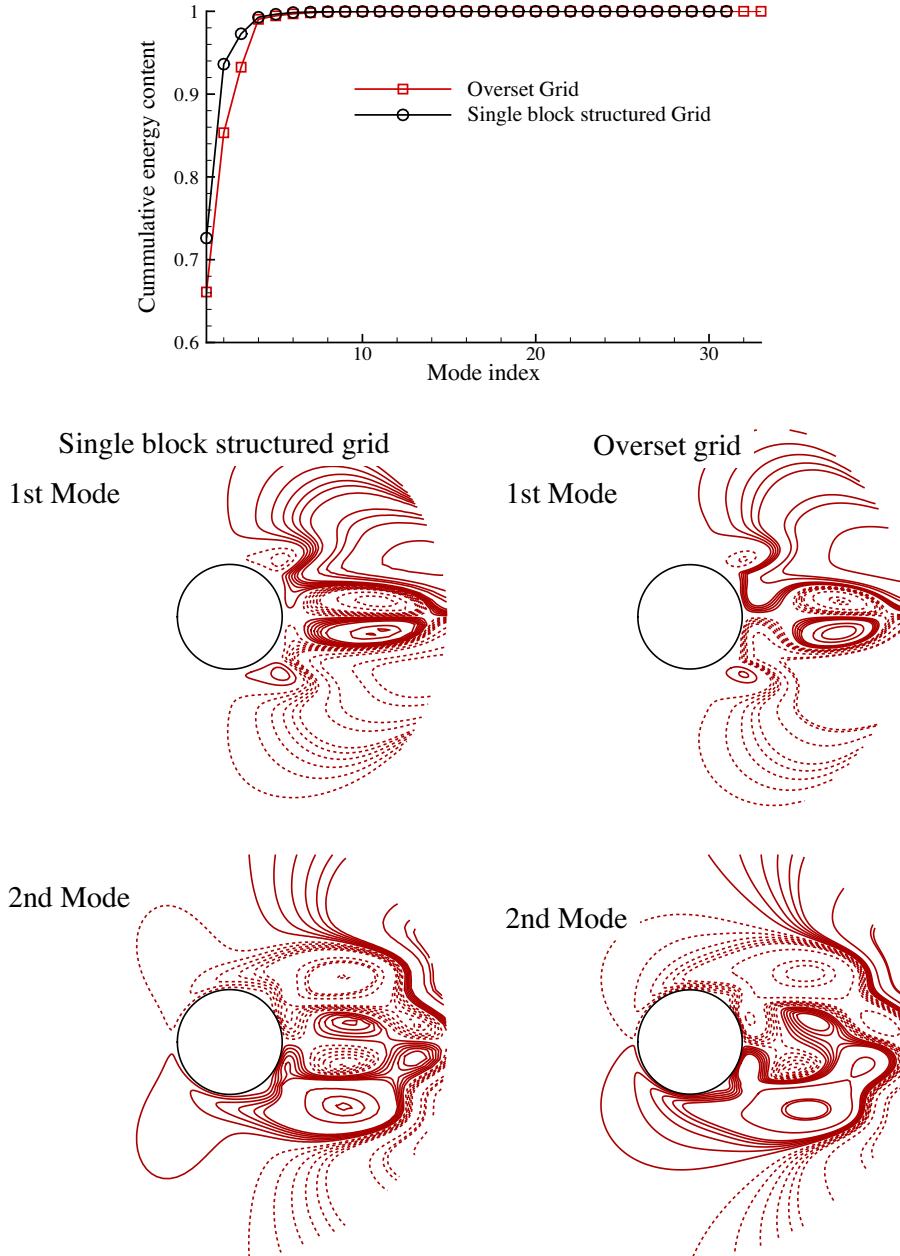

Fig. 14a. Proper orthogonal decomposition (POD) for the energy for single-block structured (left) and overset grid (right) results at *Re* = 100. The top frame shows cummulative energy content of different eigenmodes for these two grids and below are shown the first two eigenmodes. Dataset is for one cycle of variation and the POD performed on a part-domain in Ω_2 for both the cases.

It is seen above that detailed eigenmodes for the vorticity-based POD analysis for enstrophy, show very good agreement between the single-block structured grid and the overset grid computations. Next, we perform the POD analysis based on energy consideration using the two-point correlation of the computed speed in the flow field for the same flow field at $Re = 100$. On the top frame of Fig. 14(a), eigenvalues representing the cumulative energy content of various modes are shown with the mode indices. For the overset grid computations, spatial resolution is fine compared to the single-block structured grid. Furthermore, the contravariant velocity components are obtained by second order central differences on stream function values. Thus, it appears that the overset grid computation data would be more accurate as compared to the single-block structured grid results. At the same time, overset grid computations would incur some error due to interpolation. Due to a combination of these factors, one notices difference in the energy level accounted by different modes by these two methods, as shown in the top frame. For the single-block structured grid, five eigenmodes account for the same level of energy, as is given by only four eigenmodes in the overset grid calculations. As in Fig. 13, here also the POD is performed in the same truncated domain for which the pressure field was calculated for the overset grid exercise. Such differences are reflected in the various eigenmodes, as shown in Figs. 14(a) and 14(b) for the second mode onwards. The first modes appear almost similar, as they account for about 66% and 72.5% of the energy content for the overset and single-block structured data, respectively. The second mode bears lesser resemblance between the two methods, although the energy carried by these two methods are almost similar. Progressively, differences are noted in third to fifth modes. Of course, the higher modes progressively become insignificant as they carry trace amounts of energy and such differences do not imply significant variation for the data.

5. Flow past two side-by-side cylinders for $Re = 100$

This exercise is undertaken to show the ability of the overset grid method in computing more complex geometries. Schematic of various sub-domains employed in this computation is shown in the top frame of Fig. 15. The gap between
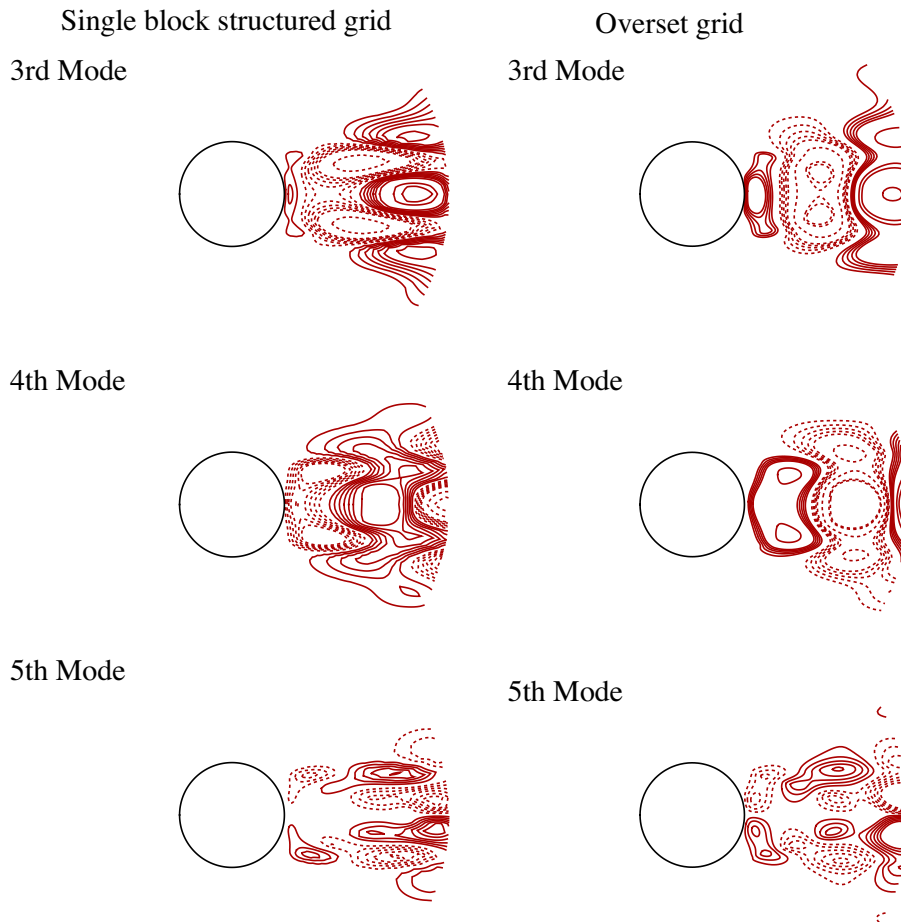

Fig. 14b. Proper orthogonal decomposition (POD) for the energy for single-block structured (left) and overset grid (right) results at $Re = 100$. The third and the fourth eigenmodes are compared here. Dataset is for one cycle of variation and the POD performed on a part-domain in Ω_2 for both the cases.
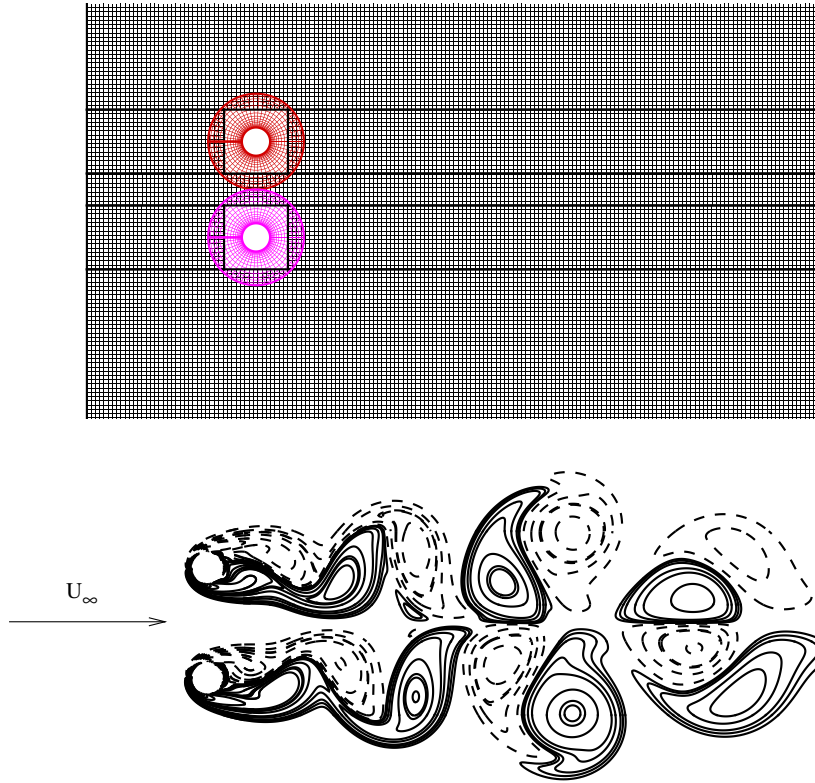
Fig. 15. The grid (top) and computed vorticity contours (bottom) for the overset method for flow past two cylinders in a side-by-side arrangement for *Re* = 100 and center to center distance of 3.4D. The top frame shows the composite grid used for the present computation; at the bottom the computed vorticity contours are displayed at *t* = 26.5.

the centers of the two cylinders is 3.4. This flow field reported in the literature [47,48] is characterized by symmetric anti-phase synchronized vortex shedding.

The grid employed in the present computations consists of 744,503 points to account for all the sub-domains. We have shown only every fifth grid line to help identify various sub-domains and their overlap clearly in Fig. 15. Starting from a uniform flow condition everywhere, Navier–Stokes equation is solved and the lower frame in Fig. 15 displays the solution at *t* = 26.5, when the lift experienced by the bottom and top cylinders are almost at their maximum magnitude. The loads are nearly anti-symmetric and this is visible in the displayed vorticity contours. Some small-scale asymmetry is noted for the vorticity field in the near-wake. Thus, the overset grid method captures the experimental attributes reported in the literature [47,48].

6. Summary

The present exercise is undertaken to develop high accuracy methods for flow past complex bodies using overset grids. In using the overset grid, additional source of error appears in the form of interpolation at sub-domain boundaries. Thus, to characterize methods for overset grids in terms of interpolation errors, we have identified flow over a single cylinder as a test problem, as detailed accurate results can be obtained using a single-block structured grid. Also, there are enough experimental evidences and results to calibrate any method for this flow. We have also computed the flow past two cylinders, in a side-by-side arrangement as an application of the overset grid method, for which one may not be able to compute the flow in a single-block structured grid with sufficient accuracy. In the computations presented here, high accuracy compact schemes have been used to discretize convection and diffusion operators. The following results have been reported in the course of this study:

(1) When the diffusion term is discretized by OUCS3 scheme for first derivative [26] twice, then this leads to higher effectiveness at smaller length scales, where one requires correct representation of the diffusion process. This is shown compared in Fig. 1 for two methods.

(2) Flow past a cylinder displays periodic shedding at a low frequency (characterized by the Strouhal number) and that can however be captured by second order central differencing (CD_2) of the dissipation terms. This aspect of the flow

Table 1
Comparison of present with other computed results for $Re = 100$.

	Single-block structured	Overset grid	Ref. [44]	Ref. [30]
Nodes	61,200	323,268	14,441	23,033
C_l'	0.23782	0.2644	0.23	0.287
$\overline{C}_d$	1.32167	1.3367	1.33	1.356
C_d'	0.00718	0.0145	0.0064	0.01
St	0.16602	0.1672	0.164	0.166

dynamics is shown in Figs. 2 and 3, that show the adequacy of CD_2 scheme for dissipation discretization. We have used this for rest of the computations reported here.

(3) The computational procedures have been further validated in Figs. 4–6 and Table 1, where the present results are compared with other computations and experiments. In doing so, we have not only compared the mean drag and shedding frequency, but we have also compared with the fluctuating lift and drag components (this has been shown in Table 1).

(4) We have developed a procedure for calculating flow past a single cylinder by using the overset grid method, the employed grids and the close-up of the sub-domain boundaries are shown in Figs. 7 and 8. Furthermore, two interpolation strategies that could be employed to transfer sub-domain boundary conditions have been studied here in greater detail in Figs. 9–11. An analytical test function that mimics convecting coherent vortices characterized by a localized Gaussian function is used here to calibrate different interpolation methods (a least square Taylor series based approach and another approach based on Lagrange interpolation) and different orders of accuracy for the former. We found that a diffused convecting structure will be better represented by a lower order least square method whereas a sharp structure is interpolated better by a higher order interpolation method. Furthermore, it is noted that the actual error (as shown in Fig. 11) is contributed by more number of points in the near vicinity of the structure for the lower order methods.

(5) The computed vorticity field by the overset grid method is shown in Fig. 12 to match excellently with the results obtained using single-block structured grid.

(6) Further finer differences between the two methods in computing the flow is demonstrated using Proper Orthogonal Decomposition in Figs. 13 and 14 for the enstrophy and energy of the flow, respectively. The vorticity field as shown by the enstrophy shows extremely good match between the two methods in Fig. 13. The match for the energy field between these two methods also shows good comparison. However, as the velocity field is obtained from the computed stream function values by CD_2 method, some differences in the higher eigenmodes are noted. This is also due to very fine mesh used in the overset grid method.

(7) Finally, flow past two cylinders in a side-by-side arrangement has been computed using the overset grid method, as shown in Fig. 15. The computed results display the expected symmetric anti-phase synchronized vortex shedding.

References

[1] A.C. Newell, Finite amplitude instabilities of partial difference equations, SIAM J. Appl. Math. 33 (1) (1977) 133.
[2] J.H. Gerrard, The wake of cylindrical bluff bodies at low Reynolds numbers, Phil. Trans. Royal Soc. Lond., Ser. A 288 (1978) 351.
[3] M.S. Bloor, The transition to turbulence in the wake of a circular cylinder, J. Fluid Mech. 19 (1964) 290.
[4] A. Kourta, H.C. Boisson, P. Chassaing, H. Haminh, Nonlinear interaction and the transition to turbulence in the wake of a circular cylinder, J. Fluid Mech. 181 (1987) 141.
[5] T. Wei, C.R. Smith, Secondary vortices in the wake of circular cylinders, J. Fluid Mech. 169 (1986) 513.
[6] M.F. Unal, J. Rockwell, On vortex formation from a cylinder. Part I. The initial instability, J. Fluid Mech. 190 (1988) 491.
[7] M. Braza, H. Persillon, F. Sers, Prediction of certain transition characteristics in the wake of a circular cylinder in free and forced flow, in: H. Eckelmann, M. Graham, P. Huerre, P. Monkewitz (Eds.), Bluff Body Wakes, Dynamics and Instabilities, Springer-Verlag, Berlin, Germany, 1993.
[8] L.D. Landau, E.M. Lifshitz, Fluid Mechanics, vol. 6, Pergamon Press, London, 1959.
[9] P.G. Drazin, W.H. Reid, Hydrodynamic Stability, Cambridge University Press, Cambridge, UK, 1981.
[10] C.P. Jackson, A finite element study of the onset of vortex shedding in flow past variously shaped bodies, J. Fluid Mech. 182 (1987) 23.
[11] A. Zebib, Stability of viscous flow past a circular cylinder, J. Eng. Math. 21 (1987) 155.
[12] M. Morzynski, F. Thiele, Numerical investigation of wake instabilities, in: H. Eckelmann, M. Graham, P. Huerre, P. Monkewitz (Eds.), Bluff Body Wakes, Dynamics and Instabilities, Springer-Verlag, Berlin, Germany, 1993.
[13] M. Golubitsky, D.G. Schaeffer, Singularities and Groups in Bifurcation Theory, Springer-Verlag, New York, 1984.
[14] L.S.G. Kovasznay, Hot-wire investigation of the wake behind cylinders at low Reynolds numbers, Proc. Royal Soc. Lond. A. 198 (1949) 174.
[15] A. Roshko, On the drag and shedding frequency of two-dimensional bluff bodies, NACA TN 3169 (1954).
[16] F. Homann, Einfluss grosser zahigkeit bei Stromung um Zylinder, Forsch. auf dem Gebeite des Ingenieurwesens. 7 (1) (1936) 1.
[17] D. Tordella, C. Cancelli, First instabilities in the wake past a circular cylinder. Comparison of transient regimes with Landau's model, Meccanica 26 (1991) 75.
[18] M. Kiya, H. Tamura, M. Arie, Vortex shedding from circular cylinder in moderate-Reynolds number shear flow, J. Fluid Mech. 141 (4) (1980) 345.
[19] M. Provansal, C. Mathis, L. Boyer, Bènard–von Kàrmàn instability: transient and forced regimes, J. Fluid Mech. 182 (1987) 1.
[20] K.R. Sreenivasan, P.J. Strykowski, D.J. Olinger, Hopf bifurcation, Landau equation and vortex shedding behind circular cylinders, in: K.N. Ghia (Ed.), Forum on Unsteady Flow Separation, vol. 1, ASME, New York, 1987, pp. 1–13.
[21] M. Nishioka, H. Sato, Mechanism of determination of the shedding frequency of vortices behind a cylinder at low Reynolds numbers, J. Fluid Mech. 89 (1978) 49.
[22] C.H.K. Williamson, Oblique and parallel modes of vortex shedding in the wake of circular cylinder at low Reynolds numbers, J. Fluid Mech. 206 (1989) 579.

[23] T.K. Sengupta, D. Das, P. Mohanamuraly, V.K. Suman, Measurement of free stream turbulence: its modeling and computations, in: Proceedings of the 16th Australasian Fluid Mech. Conf., Gold Coast, Australia, 2007.
[24] C. Norberg, Fluctuating lift on a circular cylinder: review and new measurements, J. Fluids Struct. 17 (2003) 57.
[25] R.D. Henderson, Nonlinear dynamics and pattern formation in turbulent wake transition, J. Fluid Mech. 352 (1997) 65.
[26] T.K. Sengupta, G. Ganeriwal, S. De, Analysis of central and upwind compact schemes, J. Comput. Phys. 192 (2003) 677.
[27] T.K. Sengupta, Fundamentals of Computational Fluid Dynamics, Universities Press, Hyderabad, India, 2004.
[28] S.E. Scherer, J.N. Scott, High-order compact finite-difference methods on general overset grids, J. Comput. Phys. 210 (2005) 459.
[29] G. Desquesnes, M. Terracol, E. Manoha, P. Sagaut, On the use of a high order overlapping grid method for coupling in CFD/CAA, J. Comput. Phys. 220 (1) (2006) 355.
[30] H. Ding, C. Shu, K.S. Yeo, D. Xu, Numerical simulation of flows around two circular cylinders by mesh-free least square-based finite difference methods, Int. J. Numer. Meth. Fluids 53 (2007) 305.
[31] T.K. Sengupta, T.T. Lim, S.V. Sajjan, S. Ganesh, J. Soria, Accelerated flow past a symmetric aerofoil: experiments and computations, J. Fluid Mech. 591 (2007) 255.
[32] B.R. Noack, K. Afanasiev, M. Morzynski, G. Tadmor, F. Thiele, A hierarchy of low-dimensional models for the transient and post-transient cylinder wake, J. Fluid Mech. 497 (2003) 335.
[33] A. Dipankar, T.K. Sengupta, S.B. Talla, Suppression of vortex shedding behind a circular cylinder by another control cylinder at low Reynolds numbers, J. Fluid Mech. 573 (2007) 171.
[34] P. Huerre, P.A. Monkewitz, Local and global instabilities in spatially developing flows, Ann. Rev. Fluid Mech. 22 (1990) 473.
[35] P. Huerre, M. Rossi, Hydrodynamic instabilities in open flows, in: C. Godreche, P. Manneville (Eds.), Hydrodynamics and Nonlinear Instabilities, Cambridge University Press, 1998, p. 81.
[36] W. Koch, Local instability characteristics and frequency determination of self-exited wake flows, J. Sound Vibrat. 99 (1985) 53.
[37] W. Eckhaus, Studies in Non-Linear Stability Theory, Springer-Verlag, New York, 1965.
[38] C. Wieselsberger, Neuere festellungen uber die gesetze des fluessigkeits-und luftwider- stands, Phys. Z 22 (1921) 221.
[39] U. Fey, M. Koenig, H. Eckelmann, A new Strouhal–Reynolds number relationship for the circular cylinder in the range $47 < Re < 2 \times 10^5$, Phys. Fluids 10 (7) (1998) 1547.
[40] I.H. Tuncer, Two-dimensional unsteady Navier–Stokes solution method with moving overset grid, AIAA J. 35 (3) (1997) 471.
[41] C. De Boor, A Practical Guide to Splines, Springer-Verlag, New York, 1978.
[42] C.S. Chew, K.S. Yeo, C. Shu, A generalized finite-difference (GFD) ALE scheme for incompressible flows around moving solid bodies on hybrid meshfree-Cartesian grids, J. Comput. Phys. 218 (2006) 510.
[43] Z.J. Wang, A fully conservative interface algorithm for overlapped grids, J. Comput. Phys. 122 (1995) 96.
[44] B. Sharman, F.S. Lien, L. Davidson, C. Norberg, Numerical predictions of low Reynolds number flows over two tandem circular cylinders, Int. J. Numer. Meth. Fluids 47 (2005) 423.
[45] P. Holmes, J.L. Lumley, G. Berkooz, Turbulence, Coherent Structures, Dynamical Systems and Symmetry, Cambridge University Press, UK, 1996.
[46] L. Sirovich, Turbulence and the dynamics of coherent structures. Parts 1–3, Quart. Appl. Math. 45 (1987) 561.
[47] P.W. Bearmann, A.J. Wadcock, The interaction between a pair of circular cylinders normal to a stream, J. Fluid Mech. 61 (1973) 499.
[48] M.M. Zdravkovich, Review of flow interference between two circular cylinders in various arrangements, ASME J. Fluids Eng. 99 (1977) 618.